

Water Resources Research



RESEARCH ARTICLE

10.1029/2022WR032982

Key Points:

- River hydrograph dynamics affect floodplain circulation processes
- Channel networks originating at the main river route water to the floodplain interior during sub-bankfull and overbank inundation events
- Hydraulic connectivity requires inclusion of through-bank exchange, intra-floodplain flows, and flow complexity associated topography

Supporting Information:

Supporting Information may be found in the online version of this article.

Correspondence to:

S. van der Steeg, svandersteeg@geol.sc.edu

Citation:

van der Steeg, S., Torres, R., Viparelli, E., Xu, H., Elias, E., & Sullivan, J. C. (2023). Floodplain surface-water circulation dynamics: Congaree River, South Carolina, USA. *Water Resources Research*, 59, e2022WR032982. https://doi.org/10.1029/2022WR032982

Received 6 JUN 2022 Accepted 12 OCT 2022

© 2022. The Authors.

This is an open access article under the terms of the Creative Commons Attribution-NonCommercial-NoDerivs License, which permits use and distribution in any medium, provided the original work is properly cited, the use is non-commercial and no modifications or adaptations are made.

Floodplain Surface-Water Circulation Dynamics: Congaree River, South Carolina, USA

Shailesh van der Steeg¹, Raymond Torres¹, Enrica Viparelli², Haiqing Xu³, Edwin Elias⁴, and Jessica C. Sullivan⁵

¹School of Earth, Ocean and Environment (SEOE), University of South Carolina, Columbia, SC, USA, ²Department of Civil and Environmental Engineering, University of South Carolina, Columbia, SC, USA, ³School of Natural Resources and the Environment, University of Arizona, Tucson, AZ, USA, ⁴Deltares, Delft, The Netherlands, ⁵Department of Biology & Geology, University of South Carolina Aiken, Aiken, SC, USA

Abstract A robustly calibrated and validated hydrodynamic model depicts flow patterns over a topographically complex floodplain with a heterogeneous main channel levee. Simulations highlight floodplain inundation dynamics for two conditions, the passage of sub-bankfull and overbank flood waves. Sub-bankfull inundation commences with the passage of the flood wave crest beyond the lower elevation levee breaches, and floodplain wetting is guided by the channel network. Hence, the upstream sub-bankfull inundation area expands while much of the downstream floodplain remains dry. The onset of overbank flow is spatially variable but becomes continuous, and the through-bank channels persist as preferential pathways that produce higher velocity flows several kilometers inland. Meanwhile, near-stagnant zones develop between through-bank channel mouths, where water is temporarily stored and routed to the channel network. Also, 48% of the inundation water is from the river while 52% enters the study area from the upstream floodplain. Overall, floodplain wetting and draining processes significantly influence flow direction, and characteristics of the flood wave over the floodplain surface such that a single stage in the main channel does not uniquely define floodplain flow hydraulics. Given these findings we propose that assessments of floodplain hydraulic connectivity account for the effects of heterogeneous levee structure and intra-floodplain exchanges, as well as the typical flow thresholds associated with submergence and emergence of topography.

1. Introduction

Floodplains typically are low relief but topographically complex landscapes (e.g., Lewin & Ashworth, 2014; Park, 2020; Xu et al., 2020) with a structure reflecting the range of drivers operating at different temporal and spatial scales (e.g., Dunne & Aalto, 2013; Mertes, 1997; Trigg et al., 2012). Floodplain features are readily identifiable in satellite imagery for large rivers (e.g., Mertes, 1997; Lewin & Ashworth, 2014; Rowland et al., 2009), and in data from airborne lidar for much smaller systems (e.g., David et al., 2017; Lindroth et al., 2020; Xu et al., 2020). These data reveal that floodplains often contain extensive channel networks (e.g., David et al., 2017; Fagan & Nanson, 2004; Xu et al., 2020), including networks originating with levee breaches (Day et al., 2008; Lewin & Hughes, 1980; Xu et al., 2021).

Likewise, floodplain hydraulic connectivity, defined here as the degree of surface water exchange between a river and its floodplain (e.g., Amoros & Bornette, 2002; Passalacqua, 2017; Wohl et al., 2019), can be expected to vary considerably with variations in stage (e.g., Amoros & Bornette, 2002; Czuba et al., 2019; Xu et al., 2021). For instance, floodplains may experience frequent low-magnitude floods under high, but below bankfull river stages (e.g., Day et al., 2008; Pinel et al., 2020; Xu et al., 2021) giving rise to sub-bankfull inundation. Discrete river-floodplain segments may experience the simultaneous occurrence of sub-bankfull and overbank flooding, or no flooding at all depending on heterogeneity in the along-channel and vertical structure of riverbanks and levees. The net result is highly a variable and complex floodplain flow (Xu et al., 2021), that can present abrupt current reversals (van der Steeg et al., 2021). Hence, complex flow dynamics develop in response to along-channel variations of river-floodplain coupling-decoupling, and by flow interactions with local topography. Indeed, complex floodplain flow dynamics have been reported by remote sensing (e.g., Alsdorf et al., 2007; Hamilton et al., 2007; Mertes, 1997) and by direct field observations (Filgueira-Rivera et al., 2007; Girard et al., 2009; van der Steeg et al., 2021).

VAN DER STEEG ET AL. 1 of 18

For detailed analyses of flows over a floodplain, researchers often resort to process-based hydrodynamic models (e.g., Byrne et al., 2019; Czuba et al., 2019; Pinel et al., 2020). One major advantage of numerical flow modeling is the capability to increase the spatial and temporal resolution of point-oriented field observations. If constrained with suitable field data, model results can provide near-realistic predictions of flows with high spatial and temporal resolution, which allow for hydrodynamic assessments across the model domain. Recent floodplain modeling efforts provide insight into floodplain flows, but the model constructs lack sufficient calibration to account for realistic, time-varying flow conditions (e.g., Czuba et al., 2019; Pinel et al., 2020; Tull et al., 2022). For example, Czuba et al. (2019) highlight how floodplain channels affect hydraulic connectivity under steady boundary conditions. This approach precludes the assessment of inundation dynamics of floods with highly variable stages. Similarly, Tull et al. (2022) used quasi-steady boundary conditions to demonstrate that during sub-bankfull river stages complex floodplain flows can result due to prior flooding. This approach improves on the work by Czuba et al. (2019) but it provides limited insight on flow processes because the boundary conditions fail to represent actual drivers of system dynamics, hence advances in floodplain science through numerical modeling require the application of unsteady forcing conditions. In addition to representative boundary conditions, models require careful incorporation of floodplain structure (i.e., topo-bathymetry) as part of the computational grid (e.g., Neal et al., 2012; Verwey et al., 2012; Yamazaki et al., 2012). This approach requires a priori knowledge of often overlooked floodplain channel networks (e.g., van der Steeg et al., 2021; Wohl et al., 2011; Xu et al., 2020) and a priori knowledge of flow processes.

Finally, an insightful modeling strategy also should include opportunities for "intra-floodplain" exchanges. In other words, models should have the flexibility to account for floodplain fluxes into and out of the immediate study site or domain of interest. By excluding this modeling capability, the modeler implies that flow dynamics are principally linked to river stage (Byrne et al., 2019; Czuba et al., 2019) or stage plus ponding (Tull et al., 2022).

The work presented here applies: (a) dynamic boundary conditions based on observations, (b) a entire floodplain computational domain much larger than the area of interest, (c) detailed measurements of channel bathymetry in the computational grid, and (d) a well-developed calibration and validation protocol with long term field observations. Motivation for this work is driven by a dearth of information on overall water circulation in the absence of steady state drivers. This work is also expected to highlight floodplain drainage, a poorly documented process. We hypothesize that interactions between floodplain structure and hydrograph shape result in complex floodplain inundation and drainage patterns. A robustly calibrated and validated Delft3D Flexible Mesh numerical flow model is presented, and simulations are forced to be as-realistically-as-possible (i.e., quasi-real-time) by multiple sets of observations. Model results represent synoptical, near-realistic views of high spatial and temporal resolution flow dynamics to acquire new knowledge on the characteristics of, and controls on floodplain wetting, circulation and draining.

2. Study Region and Hydrologic Conditions

The study site is the \sim 93 km² floodplain of the Congaree National Park (CNP) and the surrounding floodplain, from Columbia (Figure 1a) to the Wateree River. The entire floodplain is \sim 60 km long and on average, about 4.5 km wide, with a total area of \sim 300 km². The park has been held in conservation since the mid-1970s to aid in the preservation of the large stands of old growth tree communities (Kinzer, 2017). CNP is bound by the Congaree River to the south, bluffs to the north, and the Wateree River to the east. The floodplain has almost complete forest cover where \sim 80% of the canopy is above 10 m. Two small, upland tributary channels discharge water to CNP (Figure 1a; Xu et al., 2021), but they contribute little to the overall water prism (e.g., Doyle, 2009).

Within the park, floodplain elevation declines from 35 to 23.5 m (Figure 1b), resulting in an average valley gradient of \sim 4 × 10⁻⁴ m/m (Xu et al., 2020). The main channel consists of straight and relatively stable meandering reaches (Williams et al., 2017; Figure 1b). Channel width varies between 80 and 160 m and the reach-averaged riverbed gradient is 1.5 × 10⁻⁴ m/m. Bank and levee height are highly variable, thereby facilitating irregular inundation patterns (Xu et al., 2021). The levees in the upstream part of the study reach require high river stage for overbank inundation, while levees downstream are less developed and overbank inundation occurs at lower stages.

VAN DER STEEG ET AL. 2 of 18

19447973, 2023, 1, Downloaded from https://agupubs.onlinelibrary.wiley.com/doi/10.1029/2022WR032982 by Cochraneltalia, Wiley Online Library on [25/01/2023]. See the Terms and Conditions (https://onlinelibrary.wiley.com/derms

and-conditions) on Wiley Online Library for rules of use; OA articles

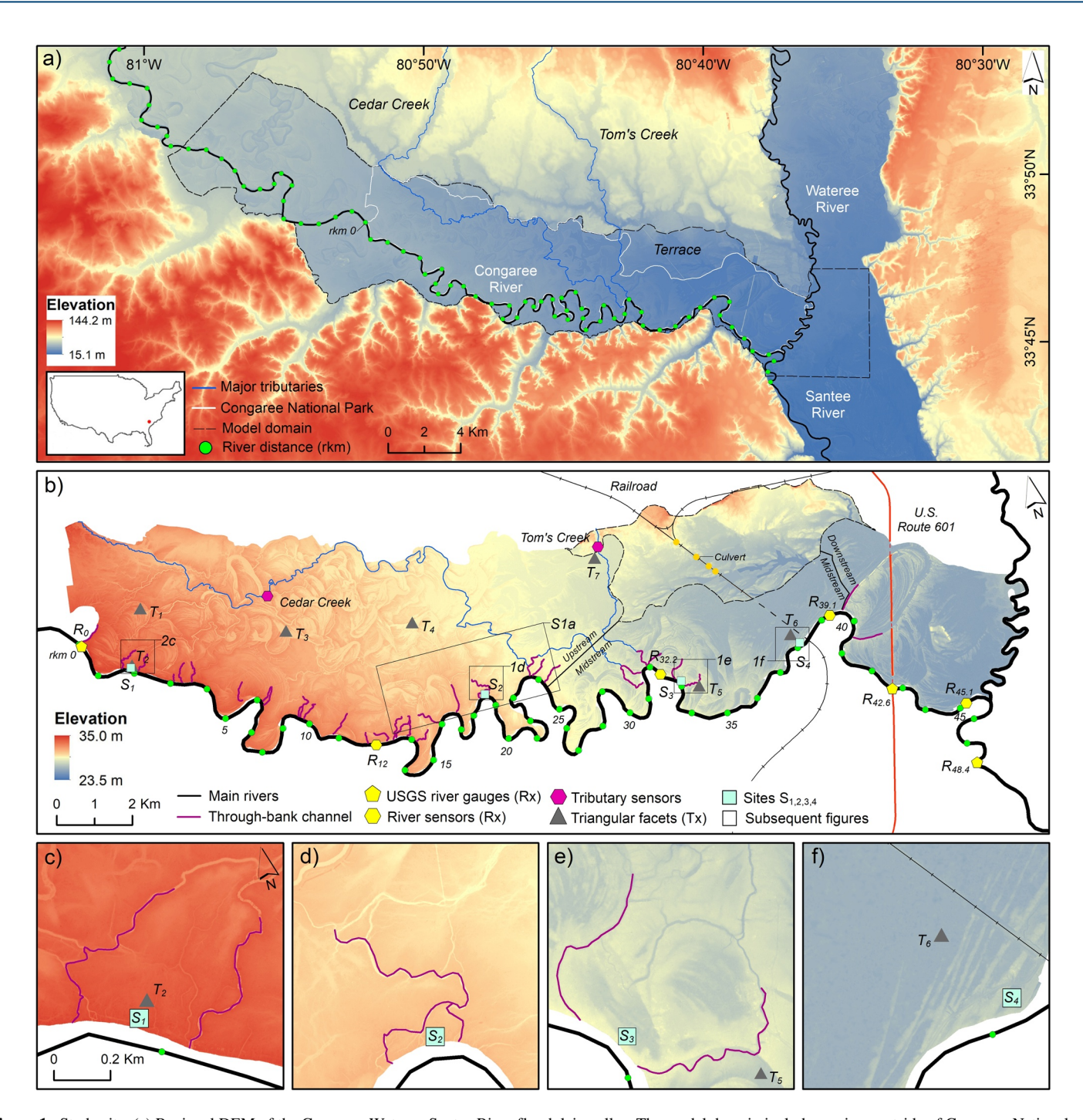


Figure 1. Study site. (a) Regional DEM of the Congaree-Wateree-Santee River floodplain valley. The model domain includes regions outside of Congaree National Park (CNP) necessary for determining accurate model results within the park. Cedar Creek and Tom's Creek are two major tributary channels. (b) DEM of Congaree National Park. The two solid lines divide the floodplain into three reaches: upstream, midstream, and downstream. (c–f) subarea of the DEM showing detailed topography surrounding the near-bank locations (S_1, S_2, S_3, S_4) .

Within the park boundary are 32 well-developed through-bank channels, having mouth widths ranging from 7 to 30 m (Xu et al., 2020, 2021; Figure 1b). Some channels are anthropogenic and extend hundreds of meters into the floodplain. Other channels are parts of natural networks that extend up to several kilometers inland (Xu et al., 2020) and thereby connect the river with an expansive network of channels, conduits and isolated depressions of the floodplain interior. Across the river from the park the local floodplain area is fragmented by active land use with agricultural dikes, ditches, and roads, comprising 19% of the total local floodplain area. This part

VAN DER STEEG ET AL. 3 of 18

of the system has limited access due to private ownership; hence, these conditions led us to focus the field observations on the much larger CNP floodplain (Figure 1).

For reference, the along channel distance is reported with the prefix "rkm" for "river kilometer," with rkm 0 at the upstream park boundary, increasing downstream. Railroad (rkm 38.3) and highway (rkm 42.6) berms are the major anthropogenic structures in the floodplain, consisting of embankment-bridge systems, that likely affect floodplain circulation during high flows (Patterson et al., 1985; Sharitz & Allen, 2009; Shelley, 2007). The railroad embankment extends 3.7 km into the floodplain, after which the bridge is supported by 4.5 by 6.8 m piers, spaced ~50 m apart that continues for 1.8 km (Figure 1b). The embankment has three 4 m high culverts that allow for water passage at times of exceptionally high flow (Kinzer, 2017). The highway embankment, locally interrupted by a pillar structure to allow for the passage of water, runs for 3.5 km into the floodplain and the pillar structure with 2.5 m diameter circular pillars, spaced ~35 m apart, continues 0.3 km (Figure 1b).

The United States Geological Survey (USGS) Congaree River gauge in Columbia, SC (#02169500) provides the nearest long-term discharge and stage records, and it is located 38 river kilometers upstream. The discharge from 1984 to 2021 ranges from 30 to 4,200 m³/s and water levels vary between 35 and 43 m. Data from the USGS Gadsden station (#02169625), rkm 0 (Figure 1b), show that since 1984 the local stage (discharge not reported) varies by 8 m. Further downstream at rkm 42.6 (Figure 1b) the USGS Highway 601 station (#02169750) was established in 2018 and records water levels and daily mean discharge only. Here, the water level signal is subdued relative to the Gadsden station; the range of 4.5 m is likely associated with poor levee development (Xu et al., 2021). Within the park, the USGS records water level at Cedar Creek (USGS Cedar Creek station, #02169672, Figure 1b). Water levels at this location are affected by both river inundation and runoff from upland source areas (Shelley et al., 2012; Xu et al., 2020). Two additional gauging stations outside of the study area provide water levels for the Santee River (USGS Santee River in Fort Motte, #02169810, rkm 48.4) and for the Wateree River (USGS Wateree River in Camden, #02148000, north of the study region, not shown Figure 1). Flood wave travel time between the Gadsden and Santee gauges (distance ~48.4 rkm) depends on stage. Sub-bankfull wave crests traverse the distance faster (49 ± 8 hr) than overbank flows $(63 \pm 3 \text{ hr})$. Inundation intervals vary across the floodplain; for sub-bankfull inundation, the wetting period is 8.4 ± 5.6 days, while for overbank exchange the period is 19.6 ± 7.7 days, and mostly during the winter and spring (Kinzer, 2017).

The floodplain structure is highly variable, but it is arranged into sections with distinct geomorphic frameworks (after Xu et al., 2021, Figure 1b): upstream (rkm 0 to 24.2), midstream (rkm 24.2 to 39.5), and downstream (rkm 39.5 to 45.3). Within these sections, four locations were selected for the analyses of flow dynamics along the riverbanks. The first site, S_1 (rkm 2.9) is at the bank in the upstream reach (Figure 1b). Two of the through-bank channels (TBCs) cut through the levees at rkm 2.7 and 3.1, surrounding the observation location, but the channels and the network are not extensive (Figure 1c). S_1 has an average elevation of 32.26 ± 0.36 m and requires higher river stage for overbank exchange to occur relative to the midstream sites. Site S_2 at rkm 18.8 is also in the upstream but at an elevation of 29.21 ± 0.34 m. Local TBCs occur at rkm 18.6 and 18.9 (Figure 1d). Site S_3 at rkm 33 is in the midstream reach but in a local depression adjacent to the main channel, and at 25.96 ± 0.3 m (Figure 1e). Likewise, TBCs occur 200 m upstream and 100 m downstream of the site. The levee near S_3 has an average crest elevation of 27.12 ± 0.41 m and the downstream TBC is directly connected to the S_3 depression via a channel network that loops around and enters the depression from the northeast. Site S_4 is also in a depression near the railroad tracks at rkm 38, at an average elevation of 24.99 ± 0.31 m (Figure 1f). S_4 has no TBCs, however, the poorly developed levee contains multiple low laying sections that allow for heterogenous sub-bankfull exchange.

3. Methods

3.1. Field Data Collection

River water depth and bank elevation at four locations along the main channel were collected using *Onset HOBO U20* absolute pressure transducers (hereafter "sensors") at rkm 12, 32.2; 39.1; and 45.1 (Figure 1b). Pressure readings were compensated for atmospheric pressure with an identical sensor deployed as a barometer. The resulting pressure readings were converted to water depth using the *Onset HOBOware* software

VAN DER STEEG ET AL. 4 of 18

suite. All water levels were converted to a common vertical reference (NAVD88) using a *Trimble R10* GPS (horizontal and vertical accuracy \pm 0.015, 0.025 m, respectively). Elevation measurements of bank height were combined with water level readings to determine the occurrence of sub-bank and overbank flow conditions (after Xu et al., 2021).

To characterize the fine scale structure of currents in response to flood waves over the floodplain in-situ measurements were collected using a total of 22 sensors. Of this set, 21 sensors were arranged in seven approximately equilateral triangles with vertices ~200 m apart (T_{1-7} ; Figure 1b). Separately, these sensors provide water level measurements at each point, and with each triangular configuration flow direction can be estimated for a ~0.1 km² area (van der Steeg et al., 2021). Furthermore, to augment the inland Cedar Creek data, one sensor was installed in Tom's Creek, a channel draining a local upland watershed (Figure 1b), and about 7 m wide.

3.2. Numerical Flow Modeling

To quantify flow dynamics and the coupling-decoupling of the river-floodplain system, the open-source Delft3D Flexible Mesh modeling suite (Delft3D FM) is used in depth-averaged mode (2D) (Deltares, 2002a, 2022b). Hydrodynamic modeling of the field site is challenging due to the highly variable inundation patterns (Xu et al., 2021), and the complex, albeit low relief topography and their interactions (e.g., Neal et al., 2012; van der Steeg et al., 2021; Yamazaki et al., 2011). Also, the dynamics of wetting and drying (Lewin & Hughes, 1980) further complicate the problem. Previous research, however, demonstrated that the process-based Delft3D FM modeling suite applied to both tidal and river wetland systems is capable of accurately simulating flow processes (e.g., Muñoz et al., 2021; Stevens et al., 2021; Straatsma & Kleinhans, 2018).

A detailed description of the model set-up for this study is provided in Text S1 in Supporting Information S1. The model was forced with unsteady discharge and water level boundary conditions obtained from USGS gauging stations (Figure 1b). Surface and bed roughness were schematized using the Manning formulation, which relates bed friction to water depth. The roughness coefficients were described during the calibration and validation process and initial estimates were guided by Arcement and Schneider (1989), and Barnes (1967). Model calibration and validation focused on the accurate representation of (a) water level in the main channel, (b) water level in the floodplain, (c) flow direction, and (d) flow gradient over the floodplain. Simulated water levels were compared with observed water levels from six locations in the river (R_{1-6} , Figure 1b), and seven locations in the floodplain (T_{1-7} , Figure 1b) for varying river discharge conditions. Simulated flow direction and gradient in the floodplain were compared to observations using the "triangular facet approach" (van der Steeg et al., 2021) for model validation. Model sensitivity for flow was examined for a range of spatially varying Manning roughness coefficients in multiple but otherwise identical simulations.

To accurately capture floodplain processes, a flexible mesh computational grid with a varying spatial resolution, guided by topo-bathymetric measurements and floodplain channel extraction (Xu et al., 2020), was constructed through a grid independence analysis, but over a much larger domain of 247 km² including the Wateree and Santee rivers, inclusive of the eastern floodplain (Figure 1a; 247 vs. 93 km²). The larger domain was required to account for "intra floodplain" water exchange (i.e., floodplain valley flows into and out of the CNP study site). Floodplain channels were delineated by higher resolution grids, guided by geomorphic floodplain feature extraction results (Figure S1 in Supporting Information S1; Xu et al., 2020). Furthermore, sensitivity testing revealed that a realistic and unsteady modeling approach using boundary conditions developed from observations is necessary to accurately represent complex floodplain flow processes. For example, the flow reversals of Figure 2 could not be reproduced in model configurations using the steady- or quasi-steady boundary conditions of Tull et al. (2022), Czuba et al. (2019), and Meitzen (2011).

Two separate calibration hydrographs were required: one for sub-bankfull (C_1 , Figure S2a in Supporting Information S1) and one for overbank (C_2 , Figure S2c in Supporting Information S1) flow processes. For C_1 , the water levels in the river are below bankfull and water enters the floodplain as through-bank (breach) flow. For C_2 water enters as both overbank and through-bank flow. A spatially varying roughness field consisting of six different Manning roughness coefficients (Text S2 in Supporting Information S1) was required to determine accurate model results, largely based on geomorphic features defined by Xu et al. (2020), and local to regional gradients. Moreover, the model was successfully validated with sub-bankfull (V_1 , Figure S2b in Supporting Information S1) and overbank (V_2 , Figure S2d in Supporting Information S1) flow events in otherwise identical

VAN DER STEEG ET AL. 5 of 18

1944/793, 2023, 1, Downloaded from https://agupubs.onlinelibrary.wiley.com/doi/10.1029/2022WR032982 by Cochraneltalia, Wiley Online Library of [2501/2023]. See the Terms and Conditions (https://onlinelibrary.wiley.com/terms-and-conditions) on Wiley Online Library for rules of use; OA articles are governed by the applicable Cree

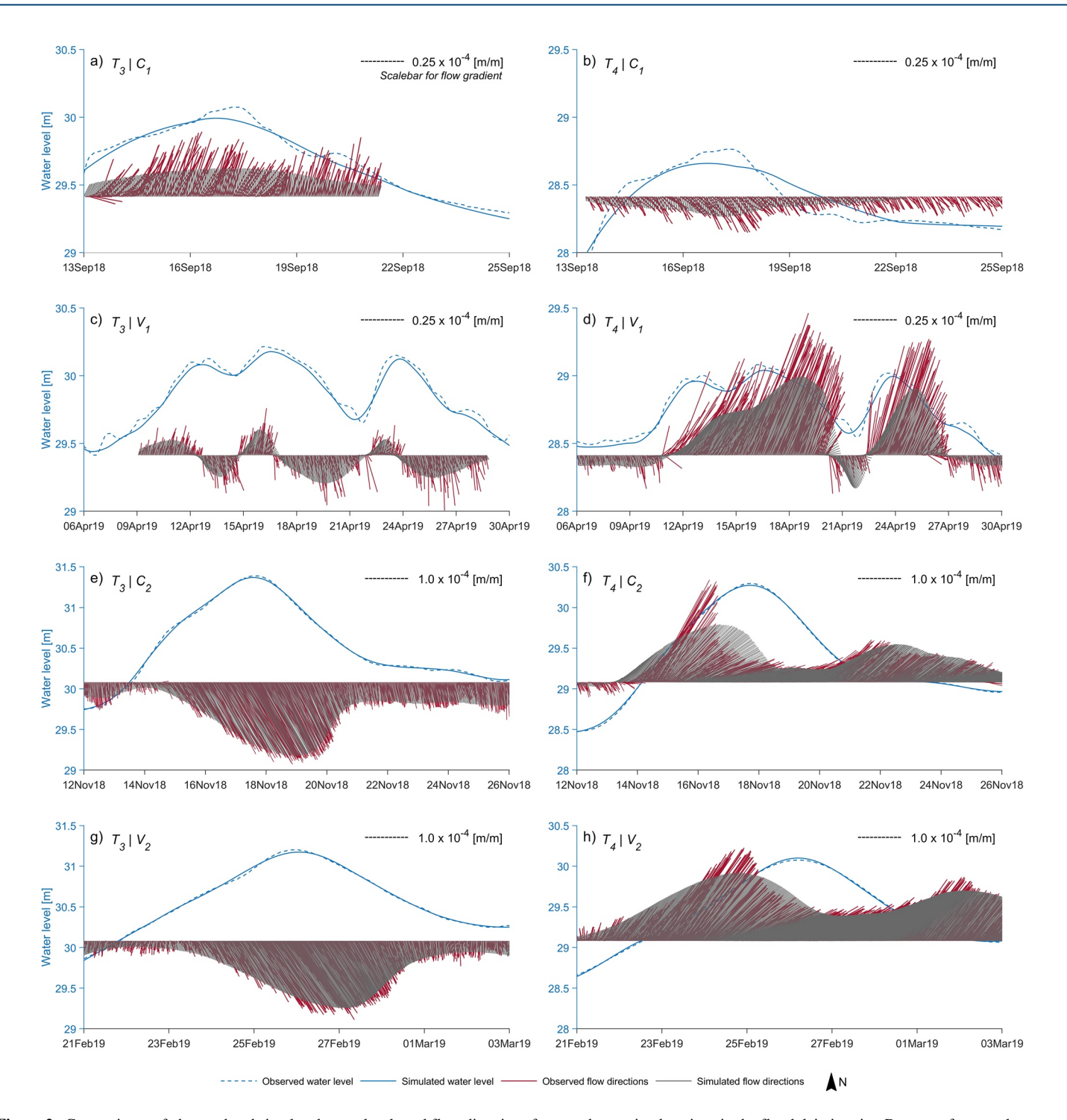


Figure 2. Comparisons of observed and simulated water levels and flow directions for two observation locations in the floodplain interior. Dates are formatted as day/month/year. Model performance for other observation sites is presented in Text S2 in Supporting Information S1. See Figure 1b for the along-channel locations of sensors. Vectors indicate magnitude and direction, with north at the top. Flows to the north are generally directed into the floodplain while flows to the south are toward the main channel. Note, due to thinning of the data, each vector represents a 2-hr interval. C_1 : lower sub-bankfull calibration scenario; V_1 : higher sub-bankfull validation scenario; C_2 : higher overbank calibration scenario; V_3 : lower overbank validation scenario.

model configurations, but model performance is better for higher flow events. Simulated water levels had an average total RMS of 0.02 ± 0.05 and 0.07 ± 0.05 m, respectively, in the river and the floodplain (Figure 2, Text S2 in Supporting Information S1). The maximum average deviation for flow directions is $39^{\circ} \pm 18^{\circ}$, while the magnitude of the free surface gradients has a maximum error of 51%.

VAN DER STEEG ET AL. 6 of 18

As with all numerical studies, the hydrodynamic model and simulation outputs have an inherent uncertainty resulting from the schematizations and approximations of real-world flow processes, and computational time restrictions that may impact the interpretation of results. Nevertheless, for the calibration and validation the model accurately represents the flow processes of interest. Also, by focusing the analyses of model results at scales beyond a single computational cell (i.e., grid-cell averaging), we show that valuable insights in floodplain flow processes can be obtained. An overview of model limitations is provided in Text S3 in Supporting Information S1.

3.3. Analyses of Floodplain Circulation

The hydrodynamic response is evaluated at high temporal resolution (15 min intervals), at multiple sites ($S_{1,2,3,4}$) near the riverbanks and in the floodplain interior (Figure 1b). The near bank sites allow us to readily differentiate between sub-bankfull and overbank exchanges, and circulation. Furthermore, these sites are representative of the spatially varying geomorphic conditions along the riverbanks, from reaches with well-developed, high gradient levees with TBCs to sections with poorly developed levees and no TBCs. Therefore, data pertaining to these sites will improve comprehension of inundation and drainage, and the influence of breaches on the dynamics of river-floodplain coupling and exchange. Their locations are fundamental elements of river-floodplain interactions (e.g., Byrne et al., 2019; Czuba et al., 2019; David et al., 2017; Tull et al., 2022) and they produce a type of "fuzzy" inundation (Xu et al., 2021). Flow vectors were averaged over 25 cells (excluding dry cells) of \sim 150 m². Averaging of flow vectors damps any spurious model outputs and ensures more representative products.

Analyses at a larger (>150 m²) spatial scale help characterize general, system-wide flow patterns during multiple events differentiated by the type of river-floodplain exchange. Both inundation extent and flow vectors (directional and velocity magnitude) were extracted from the model output. For overbank inundation events, flow vectors were aggregated (based on their means) to a coarse ~400 m grid and are only shown for inundation depths larger than 0.05 m. This decision is expected to enhance the visualization and interpretability of model results. For sub-bankfull inundation, the automatic clustering of flow vectors to a ~400 m or finer grid was inadequate for visualization and interpretation of model results. Part of the problem is related to the nature of sub-bankfull flow dynamics that occur at scales of ~20 m or smaller with floodplain channels, or 20-100 m for other floodplain features. Therefore, fine clustering will enable flow visualization at scales of 100s of meters, but for the entire CNP (1000s of meters) it would be inadequate. Thus, for sub-bankfull inundation, vectors were hand-selected and clustered to ensure relevant flow dynamics can be graphically represented. Both inundation extent (depths >0.05 m) and flow vectors were assessed at rkm -20, -10, 0, 10, 20, 30, 40, 50 with respect to the along-channel wave crest (i.e., the highest peak) propagation. By tracking the wave crest in this manner and visualizing the inundation extent and flow vectors, the model output can be managed to provide meaningful spatial and temporal coverage of flood waves through the system. Further, this approach allows for simultaneous evaluation of the rising and falling stage, and flow dynamics (e.g., flooding and drainage).

4. Results

Flow dynamics and large-scale circulation patterns were analyzed for one sub-bankfull and one overbank inundation event used to calibrate and validate the model. The results for the sub-bankfull inundation corresponds to the hydrograph for flow scenario V_1 (Figures 2c, 2d, 3a, 3b and Figure S2b in Supporting Information S1) and the overbank inundation response for C_2 (Figures 2e, 2f, 3c–3f and Figure S2c in Supporting Information S1). The near-bank results are presented using combined stage and flow vector diagrams (Figure 3); flows to the north are directed into the floodplain while flows to the south are toward the main channel. Larger-scale circulation patterns are presented using both spatially averaged flow vectors and inundation extent (Figures 4 and 5).

4.1. Near-Bank Flow Dynamics

4.1.1. Sub-Bankfull Inundation

Sub-bankfull inundation associated with V_1 is driven by a hydrograph with three crests several days apart, and water depths up to 0.9 m at the near-bank sites (Figures 3a and 3b). The rising and falling limbs are 2–3

VAN DER STEEG ET AL. 7 of 18

19447973, 2023, 1, Downloaded from https://agupubs.

.com/doi/10.1029/2022WR032982 by Cochraneltalia, Wiley Online Library on [25.01/2023]. See the Terms and Conditions (https://onlinelbrary.wiley.com/terms-and-conditions) on Wiley Online Library for rules of use; OA articles are governed by the applicable Creative Commons Licens

times steeper near the river (Figures 3a and 3b) compared to the floodplain interior (Figures 2c and 2d). During sub-bankfull inundation, only sites S_3 and S_4 experienced inundation. At S_3 (Figure 1b), on 10 April, for stages <26.62 m, the flow is initially directed to the southwest (Figure 3a). Above 26.63 m it gradually rotates ~200° clockwise to the north, and persists for ~2.5 days (10.5–13 April) with a maximum gradient of 0.52×10^{-4} on 11 April. On the falling limb of ~12 April, with stages below 26.67 m, the gradient decreases and flow rotates clockwise, to the southeast, toward a local TBC (Figure 3a, 13 April). On the rising limb of the 14 April peak, flows rotate to the north when the stage exceeds 26.62 m and persists for ~4.5 days. The higher gradients fluctuate with stage and the maximum of 0.60×10^{-4} occurs on 15 April. The 19 April falling limb, for stages from 26.58 to 26.67 m, flow rotates to the southeast and persists for ~0.5 days, but at stage <26.58 m flows gradually rotate to the northeast. The cycle between southwesterly and northerly flows on the rising limb, and between northerly, southeasterly, and northeasterly flows on the falling limb is repeated for the remainder of the hydrograph and denote an elevation threshold for flow direction.

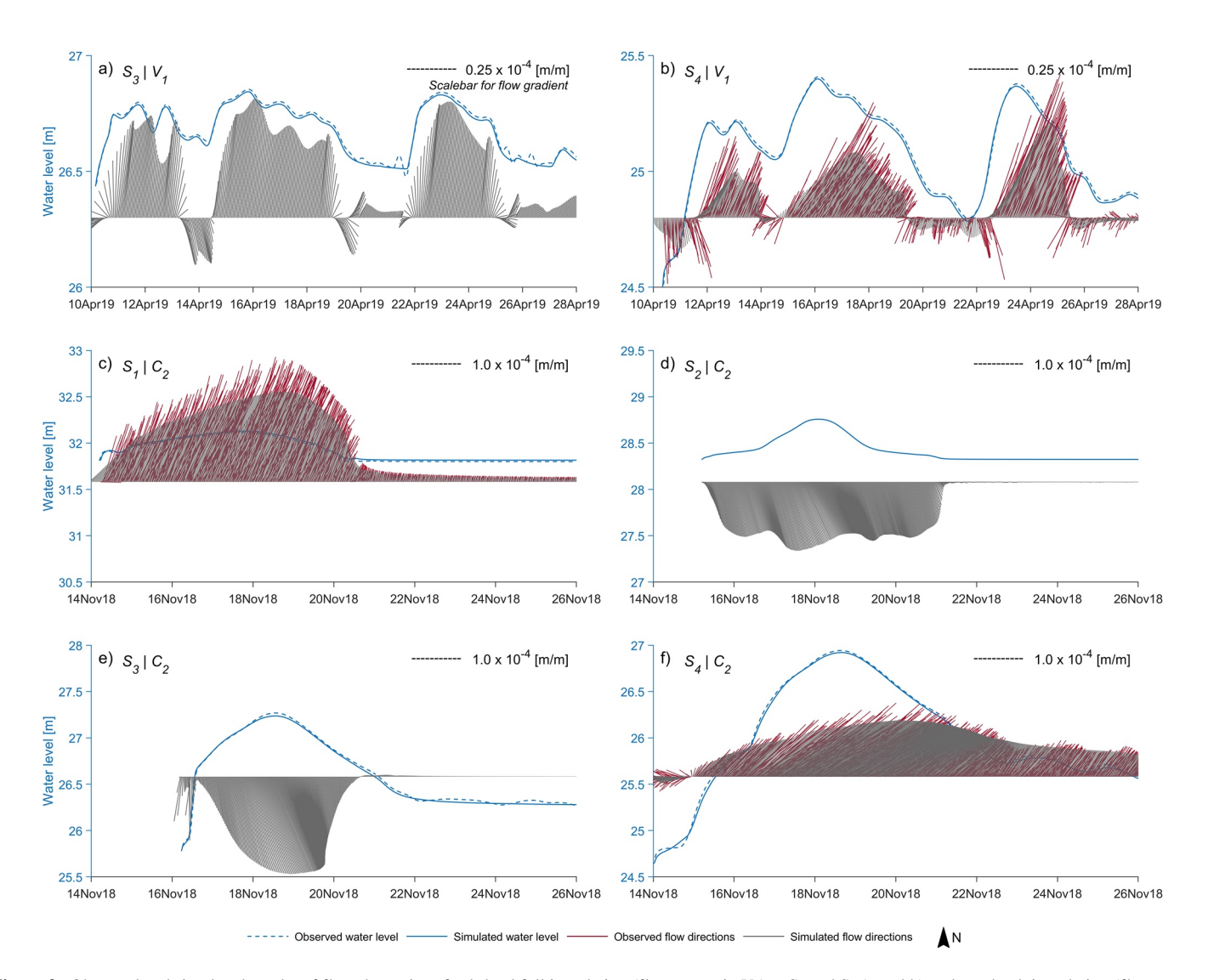


Figure 3. Observed and simulated results of flow dynamics of sub-bankfull inundation (flow scenario V_1) at S_3 and S_4 (a and b) and overbank inundation (flow scenario C_2) at S_1 , S_2 , S_3 , S_4 (c–f). Dates are formatted as day/month/year. S_2 does not show does observed flow dynamics due the absence of nearby observation sites. S_3 does not show observed flow directions due to a missing sensor. Flows to the north are generally directed into the floodplain while flows to the south are toward the main channel. Note, due to thinning of the data, each vector represents a 2-hr interval. Southward directed flows are toward the river, northward flows are to the floodplain interior. V_1 : higher sub-bankfull validation scenario; C_2 : higher overbank calibration scenario.

VAN DER STEEG ET AL. 8 of 18

Meanwhile, the S_4 site initially has flows toward the south with occasional rotations to the southeast, but with a maximum gradient of 0.16×10^{-4} (Figure 3b). On ~ 11 April, as stage approaches 24.99 m, the flow rotates toward the northeast. Here, the flow magnitude appears to be proportional to stage, with a maximum gradient of 0.26×10^{-4} occurring near peak stage. On the falling limb of the first peak on 13 April, water movement continues northeastward until the stage falls below 25.07 m, after which the general water movement is toward the southwest. The southeasterly and northeasterly flows on the rising limb, and the northeasterly and southwesterly flows on the falling limb are repeated (Figure 3b). These observations indicate that the flow reversals are stage dependent. Also, the surface gradient magnitude is strongly correlated with stage, with a maximum of 0.51×10^{-4} .

In summary, localized river-floodplain coupling by sub-bankfull inundation processes gives rise to temporally and spatially complex flow patterns associated with the submergence-emergence of local topography. For example, near-bank flows produce current reversals that depend on threshold stage height that differs for wetting or draining. At both S_3 and S_4 initial inundation occurs from the floodplain interior but above a threshold stage, flows are directed from the river to the floodplain. On the falling limbs, flows generally rotate toward the river. At both the near-bank locations (Figures 3a and 3b) and in the floodplain interior (Figures 2c and 2d) flow gradients are generally proportional to stage. The relation between stage and the occurrence of flow reversals at the near-bank locations show strong correlation but in the floodplain interior the relationship between stage and flow reversals is undefined. Taken together, the results show that flow directions are not uniquely defined by stage.

4.1.2. Overbank Inundation

When the river-floodplain system are coupled by the overbank flow process, all sites experience inundation, although the stage hydrographs and inundation depths vary substantially (Figures 3c-3f). Overbank inundation for C_2 occurs as a rise in stage from 0.5 to 2.27 m amongst the most upstream and downstream locations, respectively (Figures 3c and 3f). The rising limb close to the river is 30% steeper than at locations in the floodplain interior (Figures 2e and 2f). Similarly, recession limbs are \sim 2.5 times steeper near the bank, as observed during sub-bankfull inundation.

At the most upstream location, S_1 , overbank flow directions are consistently toward the northeast (Figure 3c), along the levee-induced topographic gradient (Figure 1b). Flow gradients are initially variable until about 14 November when the stage reaches 31.92 m. Thereafter, the gradients steadily increase and attain peak values (up to 2.0×10^{-4}) that correspond with the hydrograph peak of ~32.13 m on 17 November. The flow remains northeastward on the falling limb, until 20 November, but as the stage falls below ~31.83 m gradients decrease gradually to <0.21 \times 10⁻⁴, accompanied by a ~22° northerly rotation.

At S_2 the gradients are initially small (\sim 0.14 × 10⁻⁴) and directed toward the southeast (Figure 3d). Further along the rising stage gradients increase to 1.17×10^{-4} (16 November) and the vectors rotate gradually, >30°, toward the river. As the stage continues to increase, a short-lived rotation of >10° occurs on 17 November, at \sim 28.47 m, after which flow directions rotate back \sim 10°. Maximum gradient of 1.45×10^{-4} occurs on 18 November near the maximum stage (28.76 m). Recession starts on 18 November, with a slight counterclockwise rotation (\sim 16°) until the stage falls below \sim 28.54 m, after which the vectors attain their original directions on 20 November with a gradient of \sim 1.16 × 10⁻⁴. Thereafter, no change in flow directions occur until 21 November, and as the stage obtains values below 28.36 m flow vectors gradually rotate eastward. For stages below 28.33 m, the magnitudes decrease abruptly, but remain primarily eastward.

As with S_2 , flow directions at S_3 are primarily toward the southeast (Figure 3e), nearly perpendicular to the main channel (Figure 1b). On 16 November, as stage increases from 25.77 to 26.59 m, the steeper rising limb produces flow toward the south with occasional rotations to the southwest, with gradients reaching 0.90×10^{-4} . After 16 November, for stages exceeding 26.59 m, the rising limb vectors gradually rotate $\sim 10-30^{\circ}$ resulting in southeasterly flows that persist for ~ 2.5 days (16.5–19 November). Magnitudes increase proportionally with stage and attain a maximum value of 2.1×10^{-4} on 18 November. On the falling limb, stage is accompanied by overlapping flow vectors that continue until 19 November when stage falls below ~ 27 m. Afterward, the vectors attain their original directions while magnitude gradually decreases. On 20.5 November, for stages below ~ 26.69 m, flow directions gradually rotate $\sim 100^{\circ}$ counterclockwise, resulting in northeastward flows, and gradients decline to $< 0.03 \times 10^{-4}$.

VAN DER STEEG ET AL. 9 of 18

At S_4 (Figure 1b), a site without levees, flow is initially toward the southwest with a variable gradient reaching 0.38×10^{-4} (Figure 3f). A current reversal occurs on 15 November at ~25.03 m, near a break in the hydrograph, causing a rotation of 135°. A second break in the hydrograph on 16 November does not appear to influence flow direction. The gradient magnitudes are strongly correlated with stage, reaching 1.72×10^{-4} near the peak on 18 November. When on 22 November the stage falls below 25.76 m, the vectors slowly rotate counter-clockwise toward the northeast, and gradients remain strongly correlated with stage.

In summary, the overbank inundation process leads to varying flow directions along the riverbanks. At three locations, flow during the majority of the hydrograph is primarily directed from the river into the floodplain, while at one downstream location, the general movement of water is from the floodplain to the river, hence, this latter location is a site of floodplain drainage. As with sub-bankfull inundation, maximum gradients show strong correlation with stage. This is in general agreement with flows of the floodplain interior (Figures 2e and 2f).

4.2. River-Floodplain Coupling and Large-Scale Circulation

4.2.1. Sub-Bankfull Inundation

River-floodplain coupling starts ~2 hr after the wave crest passes the larger TBCs, therefore peaks in floodplain stage can be expected to lag river stage peaks. Flow vectors and inundation patterns indicate no substantive hydrodynamic response until the wave crest reaches rkm 10 (Figure 4a). However, with the passing of the crest the TBCs near rkm 6 become the initial source of floodwater. Flow directions are variable but mostly toward the floodplain interior. Flooding is also observed at locations where the levee is not well-developed, specifically at ~rkm 5 to 8, near a set of point bars (Figures 1 and 4).

By the time the crest reaches rkm 20, it passed 11 more TBCs, of which seven show inundation due to their low bed elevations. Corresponding flow vectors are directed into the floodplain and primarily aligned with the orientation of TBCs (Figure 4b), and again coupling initiates near bends. Meanwhile, TBCs upstream of rkm 10 continue to route river water into the floodplain, increasing the extent and depth of inundation. The general flow pattern transitions from nearly perpendicular to the river to more northwesterly - northeasterly, toward lower elevations (Figure 1b), with flow velocities limited to a maximum of 0.05 m/s and a mean of 0.03 ± 0.02 m/s (Figure 4b); the higher values are near the river-floodplain interface. These observations indicate that local storage dictates the initial flow gradients and velocity.

When the river crest reaches rkm 30 the flow and inundation fields demonstrate the ability of TBCs and connected networks to route river water across the entire floodplain. These conditions create floodplain wide hydraulic connections with the edge effects apparent as large shifts in both flow magnitude and direction; meanwhile higher velocities are aligned with the larger TBCs (Figure 4c). Moreover, the orientations of flow directions differ amongst channel networks. For example, when the flood crest is upstream of rkm 10 the flows are toward the north-northeast, but with the crest at rkm 10 to 20 flows are primarily northward, becoming northeastward when the flood crest is between rkm 20 and rkm 30 (Figure 4c). In the floodplain interior, when the flood crest is at rkm 30 flows are aligned with the floodplain channel network, indicating that TBCs and their connected networks dictate flow directions. Meanwhile, Cedar Creek becomes active and routes water to the northwestern edge of CNP, changing local flow patterns from northwest to southeastward. With this latter phase of the flood, maximum flow velocities do not necessarily occur within the channels. Both channelized and non-channelized flow speeds reach 0.12 m/s, with mean 0.08 ± 0.06 m/s.

With the crest at rkm 40 (Figure 4d) the inundation extent increases laterally, and the TBCs between rkm 30 and 40 disperse water into the floodplain. Flow velocities in TBCs upstream of rkm 30 decrease. In the region between rkm 35–38, no well-defined TBCs are identified, however, river water enters the floodplain through local, poorly developed levees and bank breaches. At some locations (rkm: 8, 9, 14–15, 21–23, 28–29, 31–32, and 35–36) flow vectors are directed from the floodplain toward the river, indicating floodplain drainage near point bars, TBCs and breaches (Figures 1 and 4d). Moreover, TBCs located within 0.5 km of the channel show both floodplain inundation and drainage patterns. For example, TBCs at rkm 31.7 and 31.8 show floodplain drainage, while the TBC at rkm 32 shows water transport into the floodplain. Besides changes in inundation extent, there appears to be a general, large scale, transport of water toward the southeast. Near the main channels, flows are aligned with local topography, but deeper into the floodplain there is an overall southeasterly flow. Hence, the TBCs distribute water from the main channel toward the floodplain interior, where water is transported

VAN DER STEEG ET AL. 10 of 18

19447973, 2023, 1, Downloaded from https://agupubs.onlinelibrary.wiley.com/doi/10.1029/2022WR032982 by Cochraneltalia, Wiley Online Library on [2501/2023]. See the Terms and Conditions (https://onlinelibrary.wiley.com/terms-and-conditions) on Wiley Online Library for rules of use; OA articles are governed by the applicable Cratic Commons License

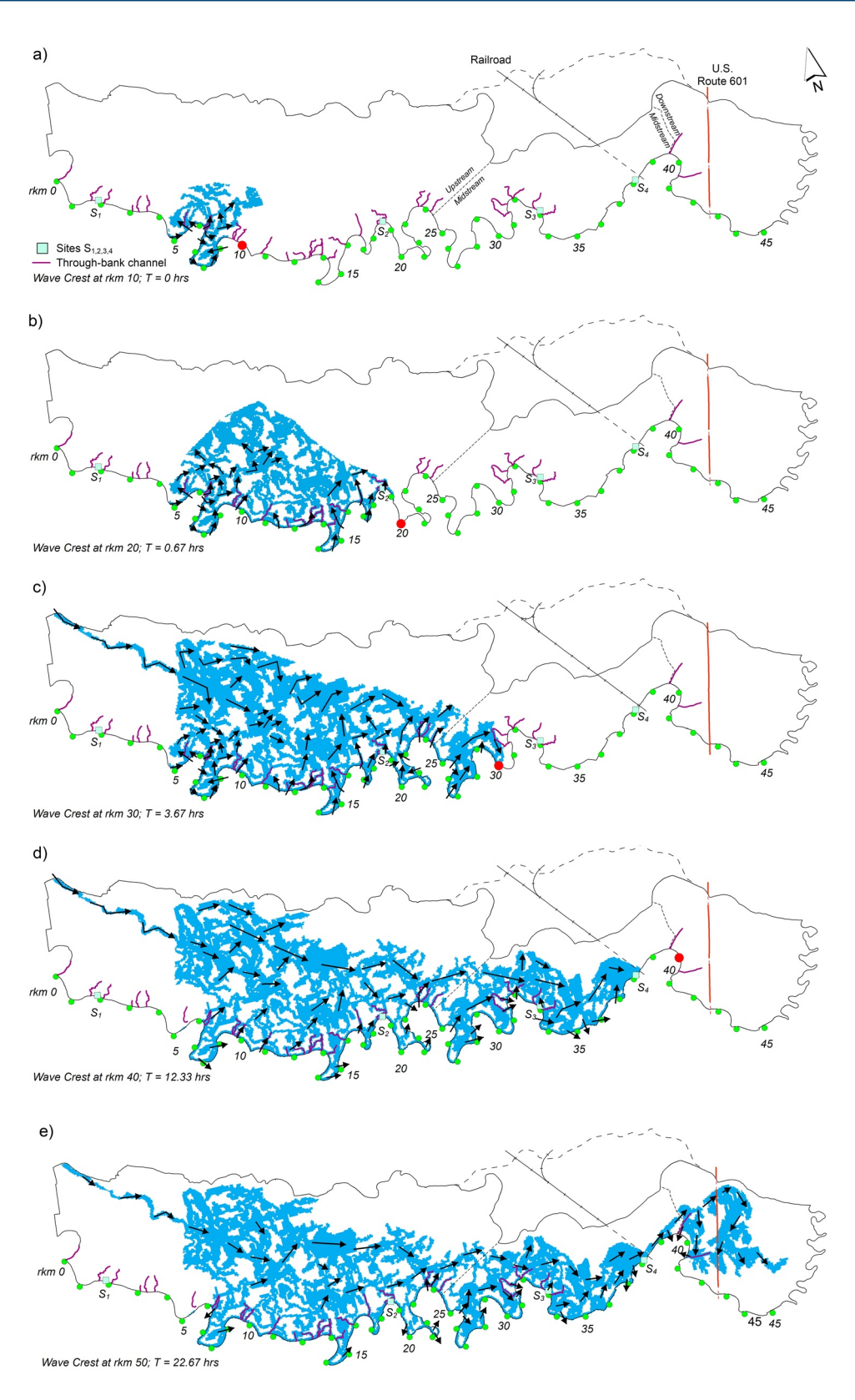


Figure 4.

VAN DER STEEG ET AL. 11 of 18

19447973, 2023, 1, Downloaded from https

downvalley. The maximum flow velocities occur in the interior and is 0.13 m/s, while the maximum velocity in TBCs near the river is 0.04 m/s; the overall mean is 0.09 ± 0.03 m/s.

With the wave crest at rkm 50, \sim 4 km downstream of the Congaree-Wateree confluence (Figure 1), the region downstream of the railroad and the highway experience inundation (Figure 4e). Between them, inundation occurs mainly near the riverbanks, while downstream of Highway 601 (Figure 1) flooding is observed in the interior and occurs via a TBC consisting of an oxbow (rkm 39.6). In the upstream reach, well-defined water transport through TBCs weakens substantially (e.g., velocities <0.03 m/s), but patterns of water transport away from the river can still be observed. Similarly, the southeastward flow observed when the wave crest was at rkm 40 weakens, but the overall flow pattern in the interior remains approximately east and southeastward. Near the riverbanks, flow vectors are locally directed toward the river. The maximum flow velocity occurs in the floodplain interior and is 0.08 m/s; while the maximum velocity in TBCs near the river are 0.03 m/s; the overall mean velocity is 0.05 \pm 0.03 m/s.

In summary, system wide sub-bankfull inundation results in local velocities that are highly variable. Flow patterns vary but depend on TBCs and their passage by the wave crest in the main channel. Initially, river water is transported into the floodplain interior along creek networks. As inundation progresses, flow patterns become southeastward near the northern inundation front. Also, TBCs transport water inland, where it is then routed southeastward. Apart from local drainage near the riverbanks, no clear drainage patterns are observed. Hence, the more distant accommodation space remained largely unfilled. The circulation vectors at or near $S_{1,2,3,4}$ are generally in agreement with the flow dynamics of near-bank locations (Figures 3a and 3b). Sites S_3 and S_4 do not show a hydrodynamic response until the wave crest arrives at rkm 40 (Figure 4d), when the general flow pattern at site S_3 is northward, but the flow at Site S_4 is northeastward. These directions are in agreement with the primary flow directions observed at the hydrograph scale at sites S_3 (Figure 4a) and S_4 (Figure 3b), and appear related to higher stages in the floodplain (peaks of local hydrographs). When the wave crest is at rkm 50 (Figure 4e), the general flow direction at S_4 and S_5 is northeastward. Site S_4 indicates local floodplain drainage toward the south. These larger-scale flow directions appear to be linked with stage recession when compared to local flow dynamics (Figures 3a and 3b). Overall, heterogeneity in river-floodplain coupling-decoupling dynamics control the local and inland patterns of circulation.

4.2.2. Overbank Inundation

Higher discharge events produce spatially variable overbank inundation at various locations along the park boundary that precedes the arrival of the river crest. For instance, with the crest at rkm -20, water enters the floodplain primarily via through-bank flow and via levee breaches (Figure 5a). In the upstream reach, TBCs transport water into the floodplain but the extent of inundation is limited. At the western park boundary, water enters the floodplain via TBCs upstream of the Gadsden gauge. Further along the river, the midstream reach experiences widespread inundation before the upstream, and TBCs transport water deep into the floodplain interior. At locations where river water reached the northern bluff several kilometers inland, the flows are deflected downvalley. The mean flow velocity across the floodplain is 0.16 ± 0.12 m/s and a maximum velocity of 0.34 m/s occurs in the midstream. Overall, flow directions near the main channel are aligned with the TBCs while deeper in the floodplain interior, specifically in the midstream reach, the flow is generally oriented toward the northeast.

With the flood crest at rkm -10 the extent of inundation continues to increase, accompanied by local velocity increases (Figure 5b). In this case, water is transferred to the floodplain as overbank flow. Also, in the upstream reach, floodwaters enter the park across the western boundary as intra-floodplain flow. In other words, the water inundating the Park arrives from the upstream floodplain, not from the river, and flow directions are variable but generally downvalley. Where floodwaters reach the northern bluffs, the flow is deflected eastward. In the midstream reach, there is simultaneous through-bank and overbank flow. Also, the local terrace, which is ~ 1 m

Figure 4. Inundation extent (blue, depths >0.05 m) and flow vectors (arrows) during sub-bankfull inundation. The flow vectors were hand-selected and aggregated from model output as automatic aggregation to a larger scale grid was inadequate to visualize sub-bankfull flow directions. The solid black line depicts the boundary of CNP. The dashed black line indicates the extent of a terrace that borders CNP. The two solid lines divide the floodplain into three reaches: upstream, midstream, and downstream. The red dot indicates the location of the wave crest. For (f) wave crest has exited the study region and is located at rkm 50, \sim 4 km downstream of the confluence. Inundation not indicated with a flow vector, occur at velocities <0.01 m/s. The straight-line inundation fronts observed in (c and d) result from limiting the visualized inundation to depths equal or greater than 0.05 m.

VAN DER STEEG ET AL. 12 of 18

1944/973, 2023, 1, Downloaded from https://agupubs.onlinelibrary.witey.com/doi/10.1029/2022WR032982by Cochraneltalia, Wiley Online Library on [2501/2023]. See the Terms and Conditions (https://onlinelibrary.viney.com/ems-and-conditions) on Wiley Online Library for rules of use; OA articles are governed by the applicable Creative Commons Licensea

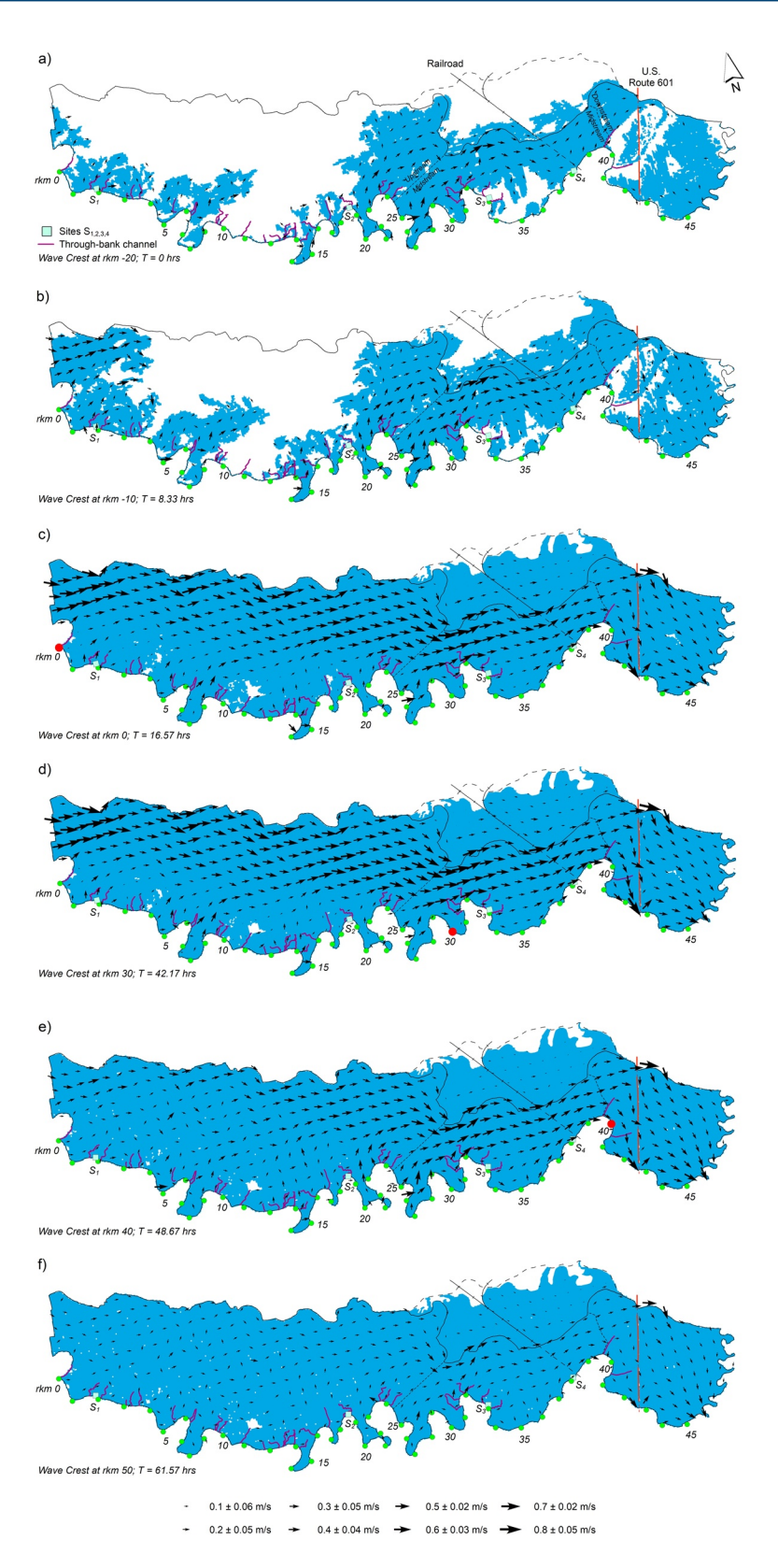


Figure 5.

VAN DER STEEG ET AL. 13 of 18

higher than the surrounding floodplain, forces flow around its perimeter. The downstream region experiences inundation from the midstream floodplain as water enters via conduits near the northern boundary at Highway 601, and levee breaches. Flow downstream of the highway, close to the river is generally directed north - northwestward, while flows near the northern park boundary are toward the south and southeast. Along the interface between the floodplain and the Wateree River, flows are north-northwestward, indicating that the Wateree River also inundates the area of interest. The maximum velocity occurs in the midstream at approximately the same location as when the flood wave crest was at rkm -20, and is 0.91 m/s, while the average is 0.16 ± 0.15 m/s.

By the time the wave crest arrives at rkm 0 the floodplain is fully inundated, except for a few small patches (Figure 5c). 52% of the total flow volume enters the CNP floodplain via the western park boundary and is transported downstream along the northern bluff. In the upstream region, water originating from the main channel is conveyed to the floodplain interior via high velocity regions near TBCs (rkm ~ 0–23). Between these high velocity water streams are relatively stagnant flow zones (rkm 3, 10, and 18) with average velocities of <0.05 m/s and this water is directed toward higher velocity streams. In the midstream reach, floodplain flows are primarily eastward; flows are not aligned with TBCs but occur approximately perpendicular to the TBCs near rkm 32. As floodwaters are transported further downstream, flows at the railroad pillar-embankment are deflected to the southeast (not visible at scale of figure). Downstream of the railroad, flows are northeastward, aligned with the northern boundary and the riverbanks to the south. Further downstream, near Highway 601, part of the flow is deflected southward by a large oxbow (Figure 1b; Xu et al., 2021) and water exits the floodplain. Additionally, floodwater passes through this area where the bridge is supported by pillars. Most of the flow that reaches the region downstream of HW601 gradually rotates toward the south-southeast and exits the floodplain at the Congaree and Wateree confluence.

It is noteworthy that during inundation, with the river crest between 0 and 30 rkm the TBCs continue to function as efficient pathways that preferentially convey water from the main river toward the northern boundary (Figures 5c and 5d), while the general circulation patterns remain relatively stable and to the southeast. For example, with the river crest between 0 and 30 rkm, variations in average flow directions are limited to 12° but the velocity decreases by a factor of ~2. On the other hand, flow paths adjust substantially with the wave crest at rkm 40 (Figure 5e). For instance, the northeastward directed flow becomes less pronounced and weakened. TBC flows continue to reach the deeper floodplain interior. However, flows in the most upstream TBCs become erratic, with poorly defined flow paths. In the midstream and downstream reaches, flow patterns remain similar to when the wave crest was at rkm 30, although an increase in current can be observed at rkm 23. Flow velocities over the terrace are relatively low (<0.04 m/s).

At rkm 50, \sim 4 km downstream of confluence, flow velocities across the floodplain weaken (Figure 5f). In the upstream, the southeastward water transport along the northern park boundary is not visible. Flow velocities decrease, and directions become erratic while the floodplain is still fully inundated, and regions of high velocity surrounding TBCs have dissipated. TBCs in the midstream reach, downstream of \sim rkm 23, continue to transport river water toward the deeper floodplain interior, but at reduced velocities. Water that is transported toward the northern boundary via TBCs is conveyed eastward where it exits the floodplain near the highway, or downstream into the Congaree and Wateree rivers.

In summary, 52% of floodwater on the study site is from the upstream floodplain, not from the local river reach. River water contributions to inundation are preferentially routed through TBC-networks, and as overbank flow. Water near the riverbanks is nearly stagnant, providing flood storage that is gradually routed to TBCs. In the midstream, at higher elevations, flow is aligned with TBCs while in the lower elevations flow is perpendicular to the TBCs for varying inundation conditions. Further downstream water eventually exits the floodplain between Highway 601 and the Wateree River. The large-scale flow vectors and small-scale flow dynamics at near-bank locations demonstrate these similarities and differences. S_1 shows overbank flow directions consistently toward the northeast and is in accordance with the system scale vectors. S_2 experiences predominantly southeastern

Figure 5. Inundation extent (blue, depths >0.05 m) and flow vectors (arrows, \geq 0.01 m/s) during overbank inundation. The flow vectors show average flow directions aggregated over an \sim 400 m grid. The solid black line depicts the boundary of Congaree National Park (CNP). The dashed black line indicates the extent of a terrace that borders CNP. The two solid lines divide the floodplain into three reaches: upstream, midstream, and downstream. The red dot indicates the location of the wave crest. For (a) wave crest is located 20 km upstream of Gadsden (rkm 0), for (b) wave crest is located 10 km upstream of Gadsden (rkm 0), and for (f) wave crest has exited the study region and is located at rkm 50, \sim 4 km downstream of the confluence. Inundation extent and flow vectors for wave crest locations rkm 10 and 20 are not shown as flow circulation patterns remain relatively stable as the flood wave propagates through the main river from rkm 0 to 30.

VAN DER STEEG ET AL. 14 of 18

flows, however, system scale flow vectors indicate eastward flows. While local and large-scale flow vectors are in disagreement at S_2 flow vectors at S_3 show consistent southeastward patterns. A rotation of flow toward the northeast is consistent with the flow reversals observed at the local scale. At the most downstream location, S_4 , large scale flow vectors are consistent with local flow dynamics. Overall, higher discharge events produce a different type of river-coupling and corresponding spatial variability in flow complexity.

5. Discussion

Floodplain flows and currents in the interior (Figure 2) and near the banks (Figure 3) can be simple or highly complex for different river stages, and topographic frameworks. Moreover, the complexity in floodplain flow is largely controlled by temporal and spatial dynamics in river-floodplain coupling-decoupling effects on inundation processes. For sub-bankfull wetting, inundation occurs primarily through large TBCs after the river wave has passed. As the channel wave crest propagates, an increasing number of TBCs become active and this enhances the routing of river water into the floodplain. The result is inundation patterns that are controlled by the orientation of floodplain channels. As inundation progresses and flow patterns evolve, a general southeastward flow develops near the center of the floodplain, where the floodplain channel network is not well developed or where the floodplain elevation is lower (Figure 4d).

At intermediate spatial scale (\sim 100 m) and temporal resolution (15 min) sub-bankfull flows are complex. Floodplain inundation occurs after the wave crest passes major TBCs (Figure 4). Flow reversals are frequent with flow orientation alternating away from and toward major TBCs (Figure 3a) or levee breaches (Figure 3b). These flows appear to be threshold dependent, with the threshold set by the elevation at which flows in the floodplain network merge and then submerge local topography. For example, site S_3 is flooded from the northeast for stages below the threshold, while for higher stages inundation occurs directly from the TBC mouth. Similar patterns are observed on the falling limb (i.e., drainage). Further, flow reversals near the banks appear to be correlated with thresholds in stage, while in the floodplain interior there does not appear to be a similar relationship (Figure 2c). Hence, for a single stage at the floodplain sites multiple flow directions were detected at the same location. These observations indicate that near the river, flow dynamics are more directly controlled by stage variations in the main channel, while in the floodplain interior the local channel network and storage effects influence circulation. Thus, for a single stage in the main channel, floodplain flows show significant temporal variability.

Inundation during overbank flows primarily starts at the midstream reach, while in the upstream, inundation is limited to TBCs because the levees are well-developed. Hence, a single discharge can give rise to three simultaneous inundation conditions, through-bank flow, overbank flow, or no flow. Later, but prior to the arrival of the wave crest, inundation is augmented by flow across the western park boundary, for example, intra-floodplain water (Figures 5a and 5b). The floodplain is fully inundated by the time the wave crest reaches the upstream edge of the study area; which is in stark contrast with the initiation of sub-bankfull inundation. Meanwhile, near the northern bluff boundary a high velocity southeastward flow develops, and along the channel some zones surrounding TBCs function as efficient pathways to transport water from the main river, inland. Also, between TBCs, low velocity zones develop and appear to store water prior to reaching the nearest TBC.

At a smaller spatial scale (\sim 100 m) and higher temporal resolution (30 min), the overall flow pattern for overbank inundation appears less complex, but flow directions differ along the banks. Flows are generally directed into the floodplain, but at one reach (rkm 18.8) flow is toward the main channel, coming from a "stagnant" zone. Maximum velocities have higher correlation with stage. System-wide, the flow vectors during overbank inundation reveal higher velocity streams near the larger TBCs. However, this is not the case where flow toward the river was observed. Overall, preferential pathways, stagnant zones, intra-floodplain transfers of water, current reversals and flows that result from heterogenous levee development create highly complex flows and connections amongst flows throughout the floodplain. Therefore, these properties combined with thee spatial and temporal variations in floodplain storage give rise to the condition that a single river stage does not uniquely define characteristic floodplain flow patterns.

Overall, floodplain flow systems can have a range of complex inundation and drainage pathways. Exactly how the temporally and spatially complex flow conditions translate to quantifying hydraulic connectivity in floodplains and wetlands remains poorly defined. Understanding the dynamics of hydraulic connectivity, taken as the degree

VAN DER STEEG ET AL. 15 of 18

Wiley Online Library on [25/01/2023]. See the Term

of surface water exchange between river-floodplain systems (Amoros & Bornette, 2002; Passalacqua, 2017; Wohl et al., 2019), typically relies on numerical models that allow for estimates of flux at the river-floodplain interface (e.g., Bryne et al., 2020; Czuba et al., 2019; Tull et al., 2022), or the temporal and spatial variability in hydraulic river-floodplain coupling-decoupling. On the other hand, at times a substantial portion of floodwater, can be expected to enter the area of interest from the floodplain upstream of the study area (e.g., Figure 5). Thus, meaningful assessments of hydraulic connectivity must account for upstream floodplain sources of water that are beyond the immediate area or river reach of interest.

This study highlights complex flows in response to floodplain wetting and draining by real flood waves. Our work underscores the need for flow models that are forced to be as-realistically-as-possible to gain insight on floodplain circulation processes. For example, numerical evaluation of river-floodplain hydraulic connectivity has been investigated with unrealistic steady or quasi-steady forcing conditions (e.g., Czuba et al., 2019; Pinel et al., 2020; Tull et al., 2022) and although the results were insightful they are not easily generalized. Here, we demonstrate the dynamic nature of hydraulic connectivity with realistic scenarios and the non-unique flow response for a given stage that must be addressed to make it a meaningful system wide metric. This is especially relevant to floodplains that function are sinks for carbon (e.g., D'Elia et al., 2017; Lininger et al., 2019; Sutfin et al., 2016), and nutrients and sediments (e.g., Fischer et al., 2019; Funk et al., 2020; Osterkamp & Hupp, 2010). Furthermore, understanding the dynamics of floodplain coupling-decoupling aids flood hazard and prediction and mitigation analyses through, for example, floodplain wave attenuation. Additionally, accurate modeling can provide robust background information on computations of river and floodplain water parameters to validate remote sensing applications, such as the Surface Water Ocean Topography mission (e.g., Pavelsky et al., 2014).

6. Conclusions

Hydrodynamic simulations of floodplain flow were conducted for two discharge events; one that led to partial floodplain inundation, and one for full inundation. Detailed analyses of flow within a smaller 93 km² part of a 247 km² computational domain were used to characterize flow patterns over the low-gradient, but topographically complex area of CNP. Quantitative analyses of model performance indicate that simulation results are representative of actual field conditions. Moreover, we found that numerically replicating these complex flows requires the application of realistic or unsteady boundary conditions with computational grids including detailed bathymetry of the main river.

Flow vector analyses show that flows can be predictably simple or complex, largely controlled by inundation process. In particular, during high, but below bankfull conditions river-floodplain coupling is limited to levee and bank breaches, or via through-bank channels, becoming more fully developed after the passing of river flood wave crest. The corresponding floodplain flow patterns are highly variable, including current reversals, and the variability appears to be dependent on thresholds in stage. Flow reversals at locations near the river show strong correlations with stage, but less so in the floodplain interior. For overbank stage conditions, expansive inundation precedes the arrival of the river wave crest due to inundation by flows from the upstream floodplain, accounting for nearly 52% of the total flow volume. Also, inundated through-bank channels operate as efficient, high velocity pathways that directly connect the river to the interior.

Data Availability Statement

The lidar data set is available from NOAA Digital Coast website at https://chs.coast.noaa.gov/htdata/lidar1_z/geoid18/data/4815. The river stage and discharge records at the USGS stations are available at https://waterdata.usgs.gov/monitoring-location/02169500 (Congaree River at Columbia, South Carolina), https://waterdata.usgs.gov/monitoring-location/02169625 (Congaree River at Congaree National Park near Gadsden, South Carolina), https://waterdata.usgs.gov/monitoring-location/02169750 (Congaree River at United States Highway 601 near Fort Motte, South Carolina), https://waterdata.usgs.gov/monitoring-location/02169810 (Santee River at Trezesvants Landing near Fort Motte, South Carolina), and https://waterdata.usgs.gov/monitoring-location/02148000 (Wateree River near Camden, South Carolina). The Delft3D Flexible Mesh Suite can be obtained via Deltares (https://www.deltares.nl/en). Field data and model output can be accessed through the HyrdoShare repository associated with this manuscript (https://doi.org/10.4211/hs.859b3b546ec749a09b15b52f2163c5f5).

VAN DER STEEG ET AL. 16 of 18

19447973, 2023, 1, Downloaded from https:/

Acknowledgments

This work was supported by NASA SC EPSCoR award NNX16AR02A and NSF CBET 1751926.

References

Alsdorf, D., Bates, P., Melack, J., Wilson, M., & Dunne, T. (2007). Spatial and temporal complexity of the Amazon flood measured from space. Geophysical Research Letters. 34(8). https://doi.org/10.1029/2007gl029447

Amoros, C., & Bornette, G. (2002). Connectivity and biocomplexity in waterbodies of riverine floodplains. Freshwater Biology, 47(4), 761–776. https://doi.org/10.1046/j.1365-2427.2002.00905.x

Arcement, G. J., & Schneider, V. R. (1989). Guide for selecting Manning's roughness coefficients for natural channels and flood plains.

Barnes, H. H. (1967). Roughness characteristics of natural channels (No. 1849). US Government Printing Office.

Byrne, C. F., Stone, M. C., & Morrison, R. R. (2019). Scalable flux metrics at the channel-floodplain interface as indicators of lateral surface connectivity during flood events. Water Resources Research, 55(11), 9788–9807. https://doi.org/10.1029/2019wr026080

Czuba, J. A., David, S. R., Edmonds, D. A., & Ward, A. S. (2019). Dynamics of surface-water connectivity in a low-gradient meandering river floodplain. Water Resources Research, 55(3), 1849–1870. https://doi.org/10.1029/2018wr023527

David, S. R., Edmonds, D. A., & Letsinger, S. L. (2017). Controls on the occurrence and prevalence of floodplain channels in meandering rivers. Earth Surface Processes and Landforms, 42(3), 460–472. https://doi.org/10.1002/esp.4002

Day, G., Dietrich, W. E., Rowland, J. C., & Marshall, A. (2008). The depositional web on the floodplain of the Fly River, Papua New Guinea. Journal of Geophysical Research, 113(F1), F01S02. https://doi.org/10.1029/2006jf000622

D'Elia, A. H., Liles, G. C., Viers, J. H., & Smart, D. R. (2017). Deep carbon storage potential of buried floodplain soils. *Scientific Reports*, 7(1), 1–7. https://doi.org/10.1038/s41598-017-06494-4

Deltares (2022a). D-Flow flexible mesh technical reference manual. Deltares.

Deltares (2022b), D-Flow flexible mesh user manual, Deltares.

Doyle, T. W. (2009). Modeling flood plain hydrology and forest productivity of Congaree Swamp (p. 46). US Geological Survey.

Dunne, T., & Aalto, R. E. (2013). Large river floodplains. In J. Shroder & E. Wohl (Eds.), *Treatise on geomorphology*, *fluvial geomorphology*, (Vol. 9, pp. 645–678). Elsevier Academic Press.

Fagan, S. D., & Nanson, G. C. (2004). The morphology and formation of floodplain-surface channels, Cooper Creek, Australia. *Geomorphology*, 60(1–2), 107–126. https://doi.org/10.1016/j.geomorph.2003.07.009

Filgueira-Rivera, M., Smith, N. D., & Slingerland, R. L. (2007). Controls on natural levee development in the Columbia River, British Columbia, Canada. Sedimentology, 54(4), 905–919. https://doi.org/10.1111/j.1365-3091.2007.00865.x

Fischer, C., Damm, C., Foeckler, F., Gelhaus, M., Gerstner, L., Harris, R., et al. (2019). The "habitat provision" index for assessing floodplain biodiversity and restoration potential as an ecosystem service—Method and application. Frontiers in Ecology and Evolution, 7, 483. https://doi.org/10.3389/fevo.2019.00483

Funk, A., Tschikof, M., Grüner, B., Böck, K., Hein, T., & Bondar-Kunze, E. (2020). Analysing the potential to restore the multi-functionality of floodplain systems by considering ecosystem service quality, quantity and trade-offs. *River Research and Applications*, 37(2), 221–232. https://doi.org/10.1002/rra.3662

Girard, P., Fantin-Cruz, I., De Oliveira, S. M. L., & Hamilton, S. K. (2009). Small-scale spatial variation of inundation dynamics in a floodplain of the Pantanal (Brazil). *Hydrobiologia*, 638(1), 223–233. https://doi.org/10.1007/s10750-009-0046-9

Hamilton, S. K., Kellndorfer, J., Lehner, B., & Tobler, M. (2007). Remote sensing of floodplain geomorphology as a surrogate for biodiversity in a tropical river system (Madre de Dios, Peru). *Geomorphology*, 89(1–2), 23–38. https://doi.org/10.1016/j.geomorph.2006.07.024

Kinzer, M. (2017). Nature's return: An environmental history of Congaree National Park. University of South Carolina Press.

Lewin, J., & Ashworth, P. J. (2014). The negative relief of large river floodplains. Earth-Science Reviews, 129, 1–23. https://doi.org/10.1016/j.earscirev.2013.10.014

Lewin, J., & Hughes, D. (1980). Welsh floodplain studies: II. Application of a qualitative inundation model. *Journal of Hydrology*, 46(1–2), 35–49. https://doi.org/10.1016/0022-1694(80)90034-7

Lindroth, E. M., Rhoads, B. L., Castillo, C. R., Czuba, J. A., Güneralp, İ., & Edmonds, D. (2020). Spatial variability in bankfull stage and bank elevations of lowland meandering rivers: Relation to rating curves and channel planform characteristics. *Water Resources Research*, 56(8), e2020WR027477. https://doi.org/10.1029/2020wr027477

Lininger, K. B., Wohl, E., Rose, J. R., & Leisz, S. J. (2019). Significant floodplain soil organic carbon storage along a large high-latitude river and its tributaries. *Geophysical Research Letters*, 46(4), 2121–2129. https://doi.org/10.1029/2018gl080996

Meitzen, K. M. (2011). Flood processes, forest dynamics, and disturbance in the Congaree River floodplain, South Carolina (Doctoral dissertation). University of South Carolina.

Mertes, L. A. (1997). Documentation and significance of the perirheic zone on inundated floodplains. Water Resources Research, 33(7), 1749–1762. https://doi.org/10.1029/97wr00658

Muñoz, D. F., Yin, D., Bakhtyar, R., Moftakhari, H., Xue, Z., Mandli, K., & Ferreira, C. (2021). Inter-model comparison of Delft3D-FM and 2D HEC-RAS for total water level prediction in coastal to inland transition zones. JAWRA Journal of the American Water Resources Association.

Neal, J., Schumann, G., & Bates, P. (2012). A subgrid channel model for simulating river hydraulics and floodplain inundation over large and data sparse areas. Water Resources Research, 48(11). https://doi.org/10.1029/2012wr012514

Osterkamp, W. R., & Hupp, C. R. (2010). Fluvial processes and vegetation—Glimpses of the past, the present, and perhaps the future. *Geomorphology*, 116(3–4), 274–285. https://doi.org/10.1016/j.geomorph.2009.11.018

Park, E. (2020). Characterizing channel-floodplain connectivity using satellite altimetry: Mechanism, hydrogeomorphic control, and sediment budget. Remote Sensing of Environment, 243, 111783. https://doi.org/10.1016/j.rse.2020.111783

Passalacqua, P. (2017). The delta connectome: A network-based framework for studying connectivity in river deltas. *Geomorphology*, 277, 50–62. https://doi.org/10.1016/j.geomorph.2016.04.001

Patterson, G. G., Whetstone, B. H., & Speiran, G. K. (1985). Hydrology and its effects on distribution of vegetation in Congaree Swamp National Monument. U.S. Geological Survey.

Pavelsky, T. M., Durand, M. T., Andreadis, K. M., Beighley, R. E., Paiva, R. C., Allen, G. H., & Miller, Z. F. (2014). Assessing the potential global extent of SWOT river discharge observations. *Journal of Hydrology*, 519, 1516–1525. https://doi.org/10.1016/j.jhydrol.2014.08.044

Pinel, S., Bonnet, M. P. S., Da Silva, J., Sampaio, T. C., Garnier, J., Catry, T., et al. (2020). Flooding dynamics within an Amazonian floodplain: Water circulation patterns and inundation duration. *Water Resources Research*, 56(1), e2019WR026081. https://doi.org/10.1029/2019wr026081

Rowland, J. C., Dietrich, W. E., Day, G., & Parker, G. (2009). Formation and maintenance of single-thread tie channels entering floodplain lakes: Observations from three diverse river systems. *Journal of Geophysical Research*, 114(F2), F02013. https://doi.org/10.1029/2008jf001073

Sharitz, R. R., & Allen, B. P. (2009). Quantify change in the old-growth forests of Congaree National Park. Final report.

Shelley, D. C. (2007). Geology, geomorphology, and tectonics of the Congaree River valley, South Carolina (Doctoral dissertation). University

VAN DER STEEG ET AL. 17 of 18

of South Carolina.



- Shelley, D. C., Werts, S., Dvoracek, D., & Armstrong, W. (2012). Blujf to blujf: A field guide to floodplain geology and geomorphology of the Lower Congaree River Valley, South Carolina. From the Blue Ridge to the Coastal Plain; Field Excursions in the Southeastern United States, 29, 67.
- Stevens, A. W., van der Steeg, S., Wherry, S. A., & Wood, T. M. (2021). Hydrodynamic model of the lower Columbia River, Oregon and Washington, 2017-2020. US Geological Survey data release.
- Straatsma, M. W., & Kleinhans, M. G. (2018). Flood hazard reduction from automatically applied landscaping measures in RiverScape, a Python package coupled to a two-dimensional flow model. *Environmental Modelling & Software*, 101, 102–116. https://doi.org/10.1016/j.envsoft.2017.12.010
- Sutfin, N. A., Wohl, E. E., & Dwire, K. A. (2016). Banking carbon: A review of organic carbon storage and physical factors influencing retention in floodplains and riparian ecosystems. Earth Surface Processes and Landforms, 41(1), 38–60. https://doi.org/10.1002/esp.3857
- Trigg, M. A., Bates, P. D., Wilson, M. D., Schumann, G., & Baugh, C. (2012). Floodplain channel morphology and networks of the middle Amazon River. Water Resources Research, 48(10), 2012WR011888. https://doi.org/10.1029/2012wr011888
- Tull, N., Passalacqua, P., Hassenruck-Gudipati, H. J., Rahman, S., Wright, K., Hariharan, J., & Mohrig, D. (2022). Bidirectional river-flood-plain connectivity during combined pluvial-fluvial events. Water Resources Research, 58(3), e2021WR030492. https://doi.org/10.1029/2021wr030492
- van der Steeg, S., Xu, H., Torres, R., Elias, E. P., Sullivan, J. C., Viparelli, E., et al. (2021). A novel method for gaining new insight on flows over inundated landscapes. *Geophysical Research Letters*, 48(20), e2021GL094190. https://doi.org/10.1029/2021gl094190
- Verwey, A., Kernkamp, H. W. J., Stelling, G. S., Tse, M. L., & Leung, W. C. (2012). Potential and application of hydrodynamic modelling on unstructured grids. In *Asian and Pacific Coasts* 2011 (pp. 1254–1261).
- Williams, T. M., Song, B., & Shelley, D. C. (2017). GIS analysis of historical maps: A case study from an 1885 survey of the Congaree River. *Mathematical and Computational Forestry & Natural-Resource Sciences*, 9(2), 3.
- Wohl, E., Brierley, G., Cadol, D., Coulthard, T. J., Covino, T., Fryirs, K. A., et al. (2019). Connectivity as an emergent property of geomorphic systems. Earth Surface Processes and Landforms, 44(1), 4–26. https://doi.org/10.1002/esp.4434
- Wohl, E., Polvi, L. E., & Cadol, D. (2011). Wood distribution along streams draining old-growth floodplain forests in Congaree National Park, South Carolina, USA. *Geomorphology*, 126(1–2), 108–120. https://doi.org/10.1016/j.geomorph.2010.10.035
- Xu, H., Torres, R., van der Steeg, S., & Viparelli, E. (2021). Geomorphology of the Congaree River floodplain: Implications for the inundation continuum. *Water Resources Research*, 57(12), e2020WR029456. https://doi.org/10.1029/2020wr029456
- Xu, H., van der Steeg, S., Sullivan, J., Shelley, D., Cely, J. E., Viparelli, E., et al. (2020). Intermittent channel systems of a low-relief, low-gradient floodplain: Comparison of automatic extraction methods. Water Resources Research, 56(9), e2020WR027603. https://doi.org/10.1029/2020wr027603
- Yamazaki, D., Kanae, S., Kim, H., & Oki, T. (2011). A physically based description of floodplain inundation dynamics in a global river routing model. Water Resources Research, 47(4), https://doi.org/10.1029/2010wr009726
- Yamazaki, D., Lee, H., Alsdorf, D. E., Dutra, E., Kim, H., Kanae, S., & Oki, T. (2012). Analysis of the water level dynamics simulated by a global river model: A case study in the amazon River. Water Resources Research, 48(9), 2012WR011869. https://doi.org/10.1029/2012wr011869

References From the Supporting Information

- Gaddy, L. L., & Smathers, G. A. (1980). The vegetation of the Congaree Swamp National Monument. Veroff Geobot. Inst. ETH, Stiftung Rubel, Zurich, 69, 171–182.
- Jolliff, J. K., Kindle, J. C., Shulman, I., Penta, B., Friedrichs, M. A., Helber, R., & Arnone, R. A. (2009). Summary diagrams for coupled hydrodynamic-ecosystem model skill assessment. *Journal of Marine Systems*, 76(1–2), 64–82. https://doi.org/10.1016/j.jmarsys.2008.05.014 Limerinos, J. T. (1970). Determination of the Manning coefficient from measured bed roughness in natural channels.
- Thompson, A. J. (1998). An ecological inventory and classification of an old-growth floodplain forest in the Southeastern United States coastal plain. Doctoral dissertation. University of Georgia.
- Willmott, C. J. (1981). On the validation of models. Physical Geography, 2(2), 184-194. https://doi.org/10.1080/02723646.1981.10642213

VAN DER STEEG ET AL. 18 of 18